ARL-TR-9047 ● SEP 2020

DEVCOM ARMY RESEARCH LABORATORY

# Modeling and Flight Dynamics of a Projectile with Nonlinear, Roll-Dependent Aerodynamics

by Joshua T Bryson, Joseph D Vasile, Benjamin C Gruenwald, Jubaraj Sahu, and Frank E Fresconi

## NOTICES

### Disclaimers

The findings in this report are not to be construed as an official Department of the Army position unless so designated by other authorized documents.

Citation of manufacturer's or trade names does not constitute an official endorsement or approval of the use thereof.

Destroy this report when it is no longer needed. Do not return it to the originator.

ARL-TR-9047 ● SEP 2020


# Modeling and Flight Dynamics of a Projectile with Nonlinear, Roll-Dependent Aerodynamics

**Joshua T Bryson, Joseph D Vasile, Benjamin C Gruenwald, Jubaraj Sahu, and Frank E Fresconi**
***Weapons and Materials Research Directorate, CCDC Army Research Laboratory***

# REPORT DOCUMENTATION PAGE

*Form Approved*
*OMB No. 0704-0188*



| 1. REPORT DATE *(DD-MM-YYYY)* | 2. REPORT TYPE | 3. DATES COVERED (From - To) |
|---|---|---|
| September 2020 | Technical Report | 1 February–1 July 2020 |

**4. TITLE AND SUBTITLE**
Modeling and Flight Dynamics of a Projectile with Nonlinear, Roll-Dependent Aerodynamics

**5a. CONTRACT NUMBER**

**5b. GRANT NUMBER**

**5c. PROGRAM ELEMENT NUMBER**

**6. AUTHOR(S)**
Joshua T Bryson, Joseph D Vasile, Benjamin C Gruenwald, Jubaraj Sahu, and Frank E Fresconi

**5d. PROJECT NUMBER**

**5e. TASK NUMBER**

**5f. WORK UNIT NUMBER**

**7. PERFORMING ORGANIZATION NAME(S) AND ADDRESS(ES)**
CCDC Army Research Laboratory
ATTN: FCDD-RLW-LE
Aberdeen Proving Ground, MD 21005

**8. PERFORMING ORGANIZATION REPORT NUMBER**
ARL-TR-9047

**9. SPONSORING/MONITORING AGENCY NAME(S) AND ADDRESS(ES)**

**10. SPONSOR/MONITOR'S ACRONYM(S)**

**11. SPONSOR/MONITOR'S REPORT NUMBER(S)**

**12. DISTRIBUTION/AVAILABILITY STATEMENT**
Approved for public release; distribution is unlimited.

**13. SUPPLEMENTARY NOTES**
ORCID ID(s): Bryson, Joshua, 0000-0002-0753-6823; Vasile, Joseph, 0000-0003-3812-6277; Sahu, Jubaraj 0000-0003-3347-4387; Gruenwald, Benjamin, 0000-0003-3968-5070

**14. ABSTRACT**
Improved maneuverability for long-range projectiles is a key technology that enables both range-extension gliding flight and agile terminal flight. Designing a projectile to have marginal stability across the flight envelope improves maneuverability and reduces requirements for the control surface and actuator. However, the static aerodynamic forces and moments can be strongly nonlinear and can vary substantially with aerodynamic roll angle at moderate to high angles of attack. This work presents an approach to model projectile aerodynamics that are strongly nonlinear with angle of attack and aerodynamic roll angle. The aerodynamic model is then exercised in a 6DoF flight simulation and the results are compared with a complimentary analysis using computational fluid dynamics coupled to rigid-body dynamics simulations. The flight behavior analysis is built up incrementally using pitch-constrained cases and pitch/yaw-constrained cases to isolate different aspects of the dynamics before moving to unconstrained flight analyses.

**15. SUBJECT TERMS**
long-range guided projectiles, aerodynamic characterization, marginal stability, roll-orientation dependent aerodynamics, computational fluid dynamics, flight dynamics, projectile simulation

| 16. SECURITY CLASSIFICATION OF: | | | 17. LIMITATION OF ABSTRACT | 18. NUMBER OF PAGES | 19a. NAME OF RESPONSIBLE PERSON |
|---|---|---|---|---|---|
| a. REPORT | b. ABSTRACT | c. THIS PAGE | | | Joshua Bryson |
| Unclassified | Unclassified | Unclassified | UU | 24 | 19b. TELEPHONE NUMBER (Include area code) (410) 306-1939 |

## Contents

## List of Figures



## List of Tables

## Acknowledgments

The authors thank Dr Jim DeSpirito from the US Army Combat Capabilities Development Command (CCDC) Army Research Laboratory (ARL) for his excellent technical review of this document, as well as general technical discussions regarding flight dynamics and aerodynamic coordinate systems.

This work was supported in part by a grant of high-performance computing time from the US Department of Defense (DOD) High Performance Computing Modernization program at the CCDC Army Research Laboratory's DOD Supercomputing Resource Center (DSRC), Aberdeen Proving Ground, Maryland and the US Army Engineer Research and Development Center DSRC, Vicksburg, Mississippi.

## 1. Introduction

Improving the maneuverability of guided munitions benefits both the terminal agility to engage imperfectly located targets and the range of the munition using gliding maneuvers.[1–3] Main drivers for projectile maneuverability include the airframe design and aerodynamics, including the careful coordination of the center of pressure (CP) and center of gravity (CG) to achieve marginal stability across the flight envelope. Active research into low-drag, high-lift airframes for both supersonic and subsonic flight regimes is improving the understanding of desirable features of the airframe design while reducing design cycle iteration time to rapidly evolve capabilities.[4] Typically, long-range projectiles are designed to be symmetric flight bodies, using low aspect ratio fins as control surfaces. At moderate to high angles of attack, the static forces and moments can vary substantially with aerodynamic roll angle.[5–8]

This research presents an approach to model projectile aerodynamics that are highly nonlinear with angle of attack, and exhibit a significant dependency on aerodynamic roll angle. The aerodynamic model is exercised in a six-degrees-of-freedom (6DoF) flight simulation, and the results are compared with a complimentary analysis using computational fluid dynamics coupled to rigid-body dynamics (CFD/RBD) simulations. The flight behavior is built up incrementally, using constrained cases that isolate pitch dynamics before moving to unconstrained flight analysis.

## 2. Airframe Description

The Laboratory Technology Vehicle (LTV) is an engineering test-bed projectile used by the US Army Combat Capabilities Development Command (CCDC) Army Research Laboratory (ARL) to experiment with various gun-launched, guided flight, and maneuver technologies. The LTV flight body was shaped through a series of optimization analyses that identified design candidates with low drag and high lift-to-drag ratios while maintaining marginal stability across the supersonic Mach regime.[9] The body is 105 mm in diameter and 10 calibers (1.05 m) in length with an 0.5 caliber, 7° boattail and has a center of gravity located at 6.0 calibers back from the nose. The projectile has a 30% ogive nose as a tradeoff between drag and payload volume, with a 10.5 mm radius-rounded nose tip. There are four low-aspect-ratio fins arrayed symmetrically around the body. The projectile is designed to be sabot-launched from an 8-inch diameter gun, with no deploying aerodynamic surfaces, which limits the fin span to 8 inches tip-to-tip. Figure 1 shows an illustration of the LTV flight body, and the mass properties are given in Table 1.

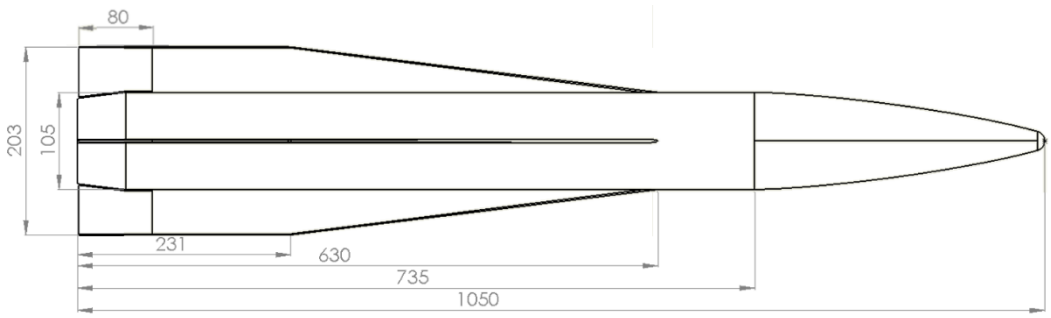


**Fig. 1 LTV flight body, with dimensions given in mm**

**Table 1 LTV mass properties**

| Mass properties | |
|---|---|
| **Mass** | 14.8 kg |
| **$CG_X$** | 630 mm from nose |
| **$CG_Y$, $CG_Z$** | on center line |
| $I_{XX}$ | 0.0273 kg-m$^2$ |
| $I_{YY}, I_{ZZ}$ | 1.17 kg-m$^2$ |

Control is provided using movable trailing edge flaps on each of the four fins, which are rotated about their leading edge. These control surfaces are sized at 80 mm chord to provide sufficient control authority to execute desired maneuvers.[9]

## 3. Flight Dynamics and Aerodynamics Models

The projectile rigid-body model has 12 states: the CG position $[x \quad y \quad z]^T$, the Euler angles describing body attitude $[\varphi \quad \theta \quad \psi]^T$, as well as the body translational velocity $[u \quad v \quad w]^T$ and rotational velocity $[p \quad q \quad r]^T$. The nonlinear 6DoF kinematic and dynamic model for the projectile flight is given in Eqs. 1–4.[10,11]

$$\begin{bmatrix}\dot{x}\\ \dot{y}\\ \dot{z}\end{bmatrix} = \begin{bmatrix}\cos\theta\cos\psi & \sin\varphi\sin\theta\cos\psi - \cos\varphi\sin\psi & \cos\varphi\sin\theta\cos\psi + \sin\varphi\sin\psi\\ \cos\theta\sin\psi & \sin\varphi\sin\theta\sin\psi + \cos\varphi\cos\psi & \cos\varphi\sin\theta\sin\psi + \sin\varphi\cos\psi\\ -\sin\theta & \sin\varphi\cos\theta & \cos\varphi\cos\theta\end{bmatrix}\begin{bmatrix}u\\ v\\ w\end{bmatrix} \quad (1)$$

$$\begin{bmatrix}\dot{\varphi}\\ \dot{\theta}\\ \dot{\psi}\end{bmatrix} = \begin{bmatrix}1 & \sin\varphi\tan\theta & \cos\varphi\tan\theta\\ 0 & \cos\varphi & -\sin\varphi\\ 0 & \dfrac{\sin\varphi}{\cos\theta} & \dfrac{\cos\varphi}{\cos\theta}\end{bmatrix}\begin{bmatrix}p\\ q\\ r\end{bmatrix} \quad (2)$$

$$\begin{bmatrix}\dot{u}\\ \dot{v}\\ \dot{w}\end{bmatrix} = \begin{bmatrix}0 & r & -q\\ -r & 0 & p\\ q & -p & 0\end{bmatrix}\begin{bmatrix}u\\ v\\ w\end{bmatrix} + \frac{1}{m}\begin{bmatrix}{}^BF_X\\ {}^BF_Y\\ {}^BF_Z\end{bmatrix} + \begin{bmatrix}-\sin\theta\\ \sin\varphi\cos\theta\\ \cos\varphi\cos\theta\end{bmatrix}g \quad (3)$$

$$\begin{bmatrix}\dot{p}\\ \dot{q}\\ \dot{r}\end{bmatrix} = [\vec{I}]^{-1}\begin{bmatrix}0 & r & -q\\ -r & 0 & p\\ q & -p & 0\end{bmatrix}[\vec{I}]\begin{bmatrix}p\\ q\\ r\end{bmatrix} + [\vec{I}]^{-1}\begin{bmatrix}{}^{B}M_{L}\\ {}^{B}M_{M}\\ {}^{B}M_{N}\end{bmatrix} \tag{4}$$

where $m$ is the mass, $[\vec{I}]$ is the inertia tensor, and $g$ is the gravitational acceleration. The $[{}^{B}F_{X} \quad {}^{B}F_{Y} \quad {}^{B}F_{Z}]^{T}$ and $[{}^{B}M_{L} \quad {}^{B}M_{M} \quad {}^{B}M_{N}]^{T}$ terms are the total aerodynamic forces and moments, respectively, in the body-fixed coordinate frame. The body-fixed coordinate frame used for the rigid-body kinematics and dynamics modeling is related to a non-rolling aerodynamic coordinate frame used for the aerodynamic modeling by the aerodynamic roll angle, $\phi_A$, as shown in Fig. 2. This non-rolling aerodynamic coordinate frame can be conceptualized as a "virtual wind tunnel" in which the aerodynamic angle is described by total angle of attack, $\bar{\alpha}$, and $\phi_A$, with $\bar{\alpha}$ always in the ${}^{A}X$-${}^{A}Z$ plane. This contrasts with the body-frame expression of the aerodynamic angles, where angle of attack, $\alpha$, describes the projection in the ${}^{B}X$-${}^{B}Z$ plane, and angle of sideslip, $\beta$, describes the ${}^{B}X$-${}^{B}Y$ plane projection.

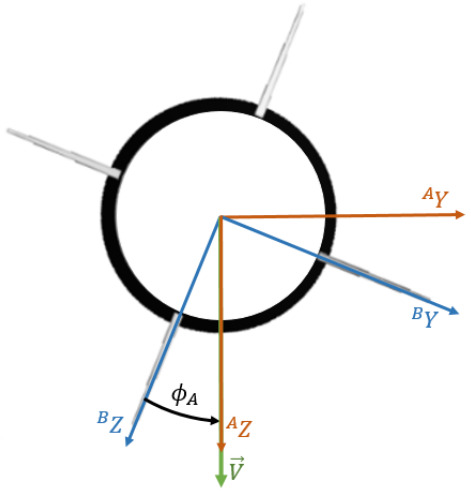


**Fig. 2 The non-rolling aerodynamic coordinate system and body-fixed coordinate system for the projectile. View is from projectile base, with both X axes into the page. The coordinate systems are related through a $\phi_A$ rotation about X, with the ${}^{B}Y$, ${}^{B}Z$ projection of the projectile translational velocity vector, $\vec{V}$, aligned to the ${}^{A}Z$ axis.**

The aerodynamic model provides the aerodynamic forces and moments at a given angle of attack and Mach number using aerodynamic coefficient data.[10,12] Aerodynamic data describing the forces and moments due to the movable fin tabs, termed movable aerodynamic surfaces (MAS), are applied separately from the aerodynamic data for the assembly of the body and fixed fin surfaces, referred to as fixed aerodynamic surfaces (FAS).

The FAS aerodynamic component model given in Eqs. 5–10 contains the aerodynamic forces and moments from the FAS in the non-rolling aerodynamic

coordinate frame, with each coefficient dependent on Mach number and aerodynamic roll angle.

$$ {}^{A}F_X^{FAS} = -QS\left[C_{A_0}(M,\phi_A) + C_{A_{\bar{\alpha}^2}}(M,\phi_A)\sin^2\bar{\alpha} + C_{A_{\bar{\alpha}^4}}(M,\phi_A)\sin^4\bar{\alpha}\right] \tag{5} $$

$$ \begin{aligned} {}^{A}F_Y^{FAS} = QS\Big[&C_{S_0}(M,\phi_A) + C_{S_{\bar{\alpha}}}(M,\phi_A)\sin\bar{\alpha} + C_{S_{\bar{\alpha}^2}}(M,\phi_A)\sin^2\bar{\alpha} \\ &+ C_{S_{\bar{\alpha}^3}}(M,\phi_A)\sin^3\bar{\alpha} + C_{S_{\bar{\alpha}^4}}(M,\phi_A)\sin^4\bar{\alpha} \\ &+ C_{S_{\bar{\alpha}^5}}(M,\phi_A)\sin^5\bar{\alpha}\Big] \end{aligned} \tag{6} $$

$$ \begin{aligned} {}^{A}F_Z^{FAS} = -QS\Big[&C_{N_0}(M,\phi_A) + C_{N_{\bar{\alpha}}}(M,\phi_A)\sin\bar{\alpha} + C_{N_{\bar{\alpha}^2}}(M,\phi_A)\sin^2\bar{\alpha} \\ &+ C_{N_{\bar{\alpha}^3}}(M,\phi_A)\sin^3\bar{\alpha} + C_{N_{\bar{\alpha}^4}}(M,\phi_A)\sin^4\bar{\alpha} \\ &+ C_{N_{\bar{\alpha}^5}}(M,\phi_A)\sin^5\bar{\alpha}\Big] \end{aligned} \tag{7} $$

$$ \begin{aligned} {}^{A}M_L^{FAS} = QSD\Big[&C_{l_0}(M,\phi_A) \\ &+ C_{l_{\bar{\alpha}}}(M,\phi_A)\sin\bar{\alpha} \\ &+ C_{l_{\bar{\alpha}^2}}(M,\phi_A)\sin^2\bar{\alpha} + C_{l_p}(M,\phi_A)\frac{pD}{2V}\Big] \end{aligned} \tag{8} $$

$$ \begin{aligned} {}^{A}M_M^{FAS} = QSD\Big[&C_{m_0}(M,\phi_A) + C_{m_{\bar{\alpha}}}(M,\phi_A)\sin\bar{\alpha} + C_{m_{\bar{\alpha}^2}}(M,\phi_A)\sin^2\bar{\alpha} \\ &+ C_{m_{\bar{\alpha}^3}}(M,\phi_A)\sin^3\bar{\alpha} + C_{m_{\bar{\alpha}^4}}(M,\phi_A)\sin^4\bar{\alpha} \\ &+ C_{m_{\bar{\alpha}^5}}(M,\phi_A)\sin^5\bar{\alpha} + C_{m_q}(M,\phi_A)\frac{qD}{2V}\Big] \end{aligned} \tag{9} $$

$$ \begin{aligned} {}^{A}M_N^{FAS} = QSD\Big[&C_{n_0}(M,\phi_A) + C_{n_{\bar{\alpha}}}(M,\phi_A)\sin\bar{\alpha} + C_{n_{\bar{\alpha}^2}}(M,\phi_A)\sin^2\bar{\alpha} \\ &+ C_{n_{\bar{\alpha}^3}}(M,\phi_A)\sin^3\bar{\alpha} + C_{n_{\bar{\alpha}^4}}(M,\phi_A)\sin^4\bar{\alpha} \\ &+ C_{n_{\bar{\alpha}^5}}(M,\phi_A)\sin^5\bar{\alpha} + C_{n_r}(M,\phi_A)\frac{rD}{2V}\Big] \end{aligned} \tag{10} $$

where $\alpha$ is the body angle of attack, $\beta$ is the body angle of sideslip, $\bar{\alpha} = \sqrt{\alpha^2+\beta^2}$ is the total body angle of attack, $D$ is the projectile diameter, $V$ is the projectile velocity, $Q = \frac{1}{2}\rho V^2$ is the dynamic pressure, and $S = \frac{\pi}{4}D^2$ is the aerodynamic reference area. The Cmq and Cnr are the pitch and yaw damping sums, which include the angular rate terms $\dot{\alpha}$ and $\dot{\beta}$ for convenience.

The MAS aerodynamic model is given in Eqs. 11–16, which sums the force and moment contributions of the four movable fin-flap surfaces arrayed around the body in the non-rolling aerodynamic coordinate frame. The MAS aerodynamic model is populated with coefficients that depend on Mach number, and the deflection angle of the $i^{th}$control surface, $\delta_i$.

$$
\begin{aligned}
{}^{A}F_X^{MAS} = & -QS\sum_{i=1}^{4}\Big[C_{A_0}^{MAS}\big(M,\delta_i,\phi_A+\phi_{MAS}^i\big) \\
& + C_{A_{\bar{\alpha}^2}}^{MAS}\big(M,\delta_i,\phi_A+\phi_{MAS}^i\big)\sin^2\bar{\alpha} \\
& + C_{A_{\bar{\alpha}^4}}^{MAS}\big(M,\delta_i,\phi_A+\phi_{MAS}^i\big)\sin^4\bar{\alpha}\Big]
\end{aligned} \tag{11}
$$

$$
\begin{aligned}
{}^{A}F_Y^{MAS} = & QS\sum_{i=1}^{4}\Big[C_{S_0}^{MAS}\big(M,\delta_i,\phi_A+\phi_{MAS}^i\big) + C_{S_{\bar{\alpha}}}^{MAS}\big(M,\delta_i,\phi_A+\phi_{MAS}^i\big)\sin\bar{\alpha} \\
& + C_{S_{\bar{\alpha}^2}}^{MAS}\big(M,\delta_i,\phi_A+\phi_{MAS}^i\big)\sin^2\bar{\alpha} \\
& + C_{S_{\bar{\alpha}^3}}^{MAS}\big(M,\delta_i,\phi_A+\phi_{MAS}^i\big)\sin^3\bar{\alpha} \\
& + C_{S_{\bar{\alpha}^4}}^{MAS}\big(M,\delta_i,\phi_A+\phi_{MAS}^i\big)\sin^4\bar{\alpha} \\
& + C_{S_{\bar{\alpha}^5}}^{MAS}\big(M,\delta_i,\phi_A+\phi_{MAS}^i\big)\sin^5\bar{\alpha}\Big]
\end{aligned} \tag{12}
$$

$$
\begin{aligned}
{}^{A}F_Z^{MAS} = & -QS\sum_{i=1}^{4}\Big[C_{N_0}^{MAS}\big(M,\delta_i,\phi_A+\phi_{MAS}^i\big) + C_{N_{\bar{\alpha}}}^{MAS}\big(M,\delta_i,\phi_A+\phi_{MAS}^i\big)\sin\bar{\alpha} \\
& + C_{N_{\bar{\alpha}^2}}^{MAS}\big(M,\delta_i,\phi_A+\phi_{MAS}^i\big)\sin^2\bar{\alpha} \\
& + C_{N_{\bar{\alpha}^3}}^{MAS}\big(M,\delta_i,\phi_A+\phi_{MAS}^i\big)\sin^3\bar{\alpha} \\
& + C_{N_{\bar{\alpha}^4}}^{MAS}\big(M,\delta_i,\phi_A+\phi_{MAS}^i\big)\sin^4\bar{\alpha} \\
& + C_{N_{\bar{\alpha}^5}}^{MAS}\big(M,\delta_i,\phi_A+\phi_{MAS}^i\big)\sin^5\bar{\alpha}\Big]
\end{aligned} \tag{13}
$$

$$
\begin{aligned}
{}^{A}M_L^{MAS} = & QSD\sum_{i=1}^{4}\Big[C_{l_0}^{MAS}\big(M,\delta_i,\phi_A+\phi_{MAS}^i\big) + C_{l_{\bar{\alpha}}}^{MAS}\big(M,\delta_i,\phi_A+\phi_{MAS}^i\big)\sin\bar{\alpha} \\
& + C_{l_{\bar{\alpha}^2}}^{MAS}\big(M,\delta_i,\phi_A+\phi_{MAS}^i\big)\sin^2\bar{\alpha} \\
& + C_{l_p}^{MAS}\big(M,\delta_i,\phi_A+\phi_{MAS}^i\big)\frac{pD}{2V}\Big]
\end{aligned} \tag{14}
$$

$$
\begin{aligned}
{}^{A}M_M^{MAS} = & QSD\sum_{i=1}^{4}\Big[C_{m_0}^{MAS}\big(M,\delta_i,\phi_A+\phi_{MAS}^i\big) + C_{m_{\bar{\alpha}}}^{MAS}\big(M,\delta_i,\phi_A+\phi_{MAS}^i\big)\sin\bar{\alpha} \\
& + C_{m_{\bar{\alpha}^2}}^{MAS}\big(M,\delta_i,\phi_A+\phi_{MAS}^i\big)\sin^2\bar{\alpha} \\
& + C_{m_{\bar{\alpha}^3}}^{MAS}\big(M,\delta_i,\phi_A+\phi_{MAS}^i\big)\sin^3\bar{\alpha} \\
& + C_{m_{\bar{\alpha}^4}}^{MAS}\big(M,\delta_i,\phi_A+\phi_{MAS}^i\big)\sin^4\bar{\alpha} \\
& + C_{m_{\bar{\alpha}^5}}^{MAS}\big(M,\delta_i,\phi_A+\phi_{MAS}^i\big)\sin^5\bar{\alpha} \\
& + C_{m_q}^{MAS}\big(M,\delta_i,\phi_A+\phi_{MAS}^i\big)\frac{qD}{2V}\Big]
\end{aligned} \tag{15}
$$

$$
\begin{aligned}
{}^{A}M_N^{MAS} = & QSD\sum_{i=1}^{4}\Big[C_{n_0}^{MAS}\big(M,\delta_i,\phi_A+\phi_{MAS}^i\big) + C_{n_{\bar{\alpha}}}^{MAS}\big(M,\delta_i,\phi_A+\phi_{MAS}^i\big)\sin\bar{\alpha} \\
& + C_{n_{\bar{\alpha}^2}}^{MAS}\big(M,\delta_i,\phi_A+\phi_{MAS}^i\big)\sin^2\bar{\alpha} \\
& + C_{n_{\bar{\alpha}^3}}^{MAS}\big(M,\delta_i,\phi_A+\phi_{MAS}^i\big)\sin^3\bar{\alpha} \\
& + C_{n_{\bar{\alpha}^4}}^{MAS}\big(M,\delta_i,\phi_A+\phi_{MAS}^i\big)\sin^4\bar{\alpha} \\
& + C_{n_{\bar{\alpha}^5}}^{MAS}\big(M,\delta_i,\phi_A+\phi_{MAS}^i\big)\sin^5\bar{\alpha} \\
& + C_{n_r}^{MAS}\big(M,\delta_i,\phi_A+\phi_{MAS}^i\big)\frac{rD}{2V}\Big]
\end{aligned} \tag{16}
$$

The roll angle location of movable surface $i$ is given by $\phi_{MAS}^i$, with $\phi_{MAS}^i = [\,0°, 90°, 180°, 270°]$ for $\delta_1, \delta_2, \delta_3, \delta_4$, respectively, as illustrated in Fig. 3.

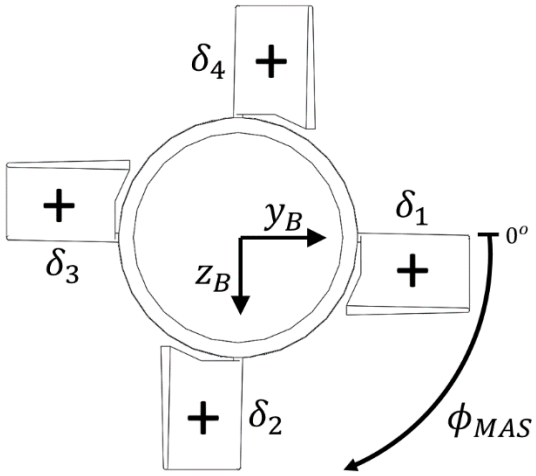


**Fig. 3 Numbering scheme of the movable aerodynamic surfaces, along with the deflection sign convention. View is from projectile base.**

Once the forces and moments for the FAS and MAS have been calculated, they are summed together into the total aerodynamic forces and moments and then rotated into the body-fixed coordinate frame, as given in Eqs. 17 and 18:

$$\begin{bmatrix} {}^{B}F_X \\ {}^{B}F_Y \\ {}^{B}F_Z \end{bmatrix} = R_X(\phi_A) \begin{bmatrix} {}^{A}F_X^{FAS} + {}^{A}F_X^{MAS} \\ {}^{A}F_Y^{FAS} + {}^{A}F_Y^{MAS} \\ {}^{A}F_Z^{FAS} + {}^{A}F_Z^{MAS} \end{bmatrix} \tag{17}$$

$$\begin{bmatrix} {}^{B}M_L \\ {}^{B}M_M \\ {}^{B}M_N \end{bmatrix} = R_X(\phi_A) \begin{bmatrix} {}^{A}M_L^{FAS} + {}^{A}M_L^{MAS} \\ {}^{A}M_M^{FAS} + {}^{A}M_M^{MAS} \\ {}^{A}M_N^{FAS} + {}^{A}M_N^{MAS} \end{bmatrix} \tag{18}$$

Where $R_X(\phi_A)$ is the rotation matrix about the X axis for the $\phi_A$ angle as given in Eq. 19:

$$R_X(\phi_A) = \begin{bmatrix} 1 & 0 & 0 \\ 0 & \cos(\phi_A) & -\sin(\phi_A) \\ 0 & \sin(\phi_A) & \cos(\phi_A) \end{bmatrix} \tag{19}$$

## 4. Aerodynamics Analysis

A full aerodynamic characterization of the vehicle was performed using a combination of semi-empirical aerodynamic prediction, inviscid CFD, and Navier-Stokes CFD.[13,14] These aerodynamic data are used to populate the coefficients in the aerodynamic model presented in Eqs. 5–16.

The projectile is designed to be marginally stable at Mach 2 to improve maneuverability and reduce the demands on the control surfaces and actuator systems. Figure 4 plots the total pitch moment (FAS+MAS) with no control surface deflections across $\bar{\alpha}$ at Mach 2 for different $\phi_A$ angles in the non-rolling aerodynamic coordinate frame. In this plot, the $C_m > 0$ region is a destabilizing condition, while $C_m < 0$ is stable; the steady state trim condition occurs where $C_m = 0$. As seen in the plot, the projectile is unstable at lower angles of attack, and stable at higher angles of attack. The projectile stability also varies across $\phi_A$, with $\phi_A = 0°$ more stable than $\phi_A = 45°$. Likewise, the trim angle for the projectile varies with $\phi_A$, with the projectile trimming at $\bar{\alpha} = 4°$ at $\phi_A = 0°$, and $\bar{\alpha} = 6°$ at $\phi_A = 45°$.

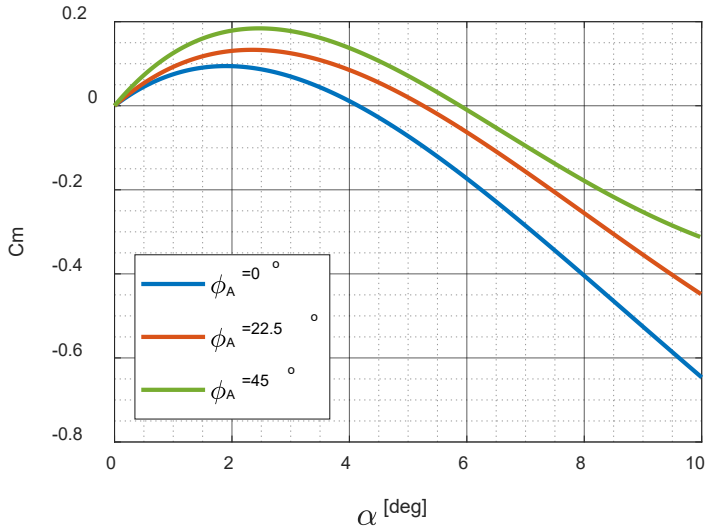


**Fig. 4 Roll angle variation in pitching moment across angle of attack at Mach 2**

Figure 5 shows the total aerodynamic force and moment coefficients (FAS+MAS) in the non-rolling aerodynamic coordinate frame for varying $\phi_A$ at Mach 2 and $\bar{\alpha} = 5°$ with no control surface deflections. Following the same trends observed in Fig. 4, the $C_m$ curve shows the projectile is stable at $\bar{\alpha} = 5°$ when $\phi_A = 0°, 90°, 180°$, and transitions to being unstable when $\phi_A = 45°, 135°$.

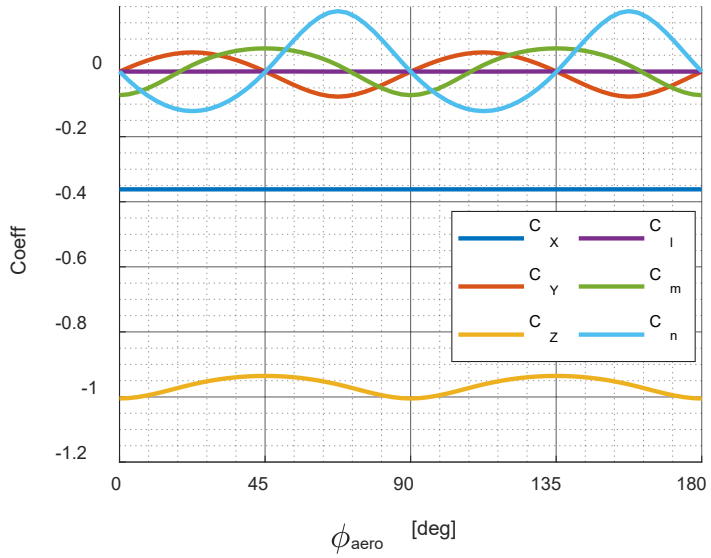


**Fig. 5 Aerodynamic force and moment coefficients for Mach 2, $\bar{\alpha} = 5°$ in the non-rolling aerodynamic frame. Note the $C_m$ value oscillates between negative (stable) and positive (unstable) with varying $\phi_A$.**

## 5. Flight Dynamics Analysis

### 5.1 Modeling Approach

The aerodynamic model from Eqs. 5–16 is combined with the rigid-body equations of motion from Eqs. 1–4 in a 6DoF flight simulation to explore the projectile flight dynamics. The output of the 6DoF flight simulation with modeled aerodynamics is compared to CFD coupled with a rigid-body dynamics routine (CFD/RBD) at specific cases of interest.

In the coupled CFD/RBD procedure, the forces and moments are computed every CFD time step and transferred to an RBD module that computes the body's response to the aerodynamic forces and moments. The response is converted into translational and rotational accelerations that are integrated to obtain translational and rotational velocities and integrated once more to obtain linear position and angular orientation. This coupled analysis technique provides both the unsteady aerodynamics and the flight dynamics in an integrated manner. Flow fields, pressure distributions, forces and moments on various surfaces, and the complete 12-state RBD history are available from the coupled solutions.

A time-accurate numerical approach is used in the coupled CFD/RBD simulations. This approach requires that the rigid-body dynamics[15] be computed at each repetition of a flow solver. The CFD capability used here solves the full Navier-Stokes equations and incorporates advanced boundary conditions and grid motion

capabilities. A commercially available code, CFD++,[16,17] is used and 3-D, time-dependent Reynolds-averaged Navier-Stokes (RANS) equations are solved using the following finite volume method.

The CFD/RBD analysis automatically takes into account the flow interactions during the flight, and yields a wealth of data unavailable in experimental methods, but it does involve highly computer-intensive calculations requiring large computational resources. The 6DoF flight simulation with modeled aerodynamics is significantly faster and less expensive to run, and can be used to quickly explore a wide range of flight conditions/behaviors, provided the modeled aerodynamics accurately represent the true behavior. Typically, the CFD/RBD analysis is compared to the 6DoF simulation at a small number of specific cases of interest as a benchmark to ensure agreement, allowing the 6DoF to be used for additional analyses with confidence.

The following sections present simulation results of the LTV using both 6DoF and CFD/RBD analysis. The cases build from more isolated, constrained flight behaviors into more integrated test cases to illustrate the major drivers of the dynamics. Finally, an analysis of fully unconstrained 6DoF flight simulations is presented.

## 5.2 Pitch-Constrained Flight

The LTV is simulated using both the 6DoF flight simulation and the CFD/RBD method with the dynamics constrained to focus only on the pitching moment contribution. Two cases are analyzed at velocity of Mach 2, with $\phi_A$ set to both $0°$ and $45°$. In both cases the projectile was initialized with a 4 rad/s pitch rate to excite the pitch dynamics. The conditions for the two pitch-constrained simulations are given in Table 2.

**Table 2 Conditions for pitch-constrained simulations**

| | Initial conditions | | Aero forces and moments |
|---|---|---|---|
| Case 1 | $\phi_A = 0°$ | $q_0 = 4$ [rad/s] | $C_m$ only |
| Case 2 | $\phi_A = 45°$ | $q_0 = 4$ [rad/s] | $C_m$ only |

The simulation results for Case 1 are shown in Fig. 6. The initial $q$ causes the projectile to pitch up to $10°$ first peak and the magnitude is sufficient to cause the projectile to oscillate back and forth between positive and negative $\alpha$ as the motion gradually damps out. Over time, the projectile begins damping towards a steady state $\bar{\alpha}$ of about $4°$, as expected from the trim analysis for $\phi_A = 0°$ from Fig. 4.

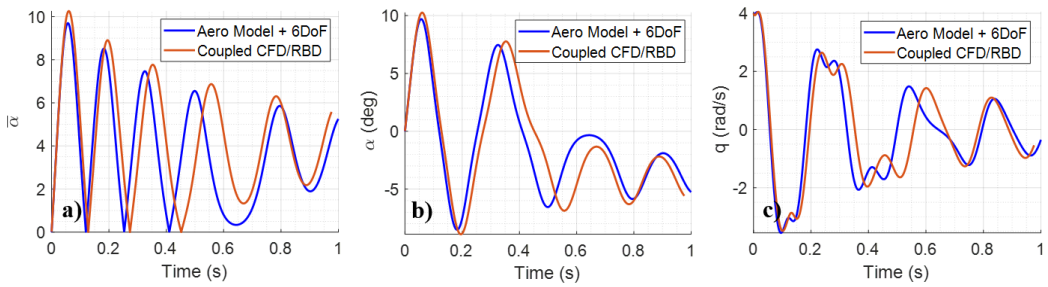


**Fig. 6 Flight simulation results for Case 1 at $\phi_A = 0°$, with $\bar{\alpha}$ vs. time plotted in a), $\alpha$ vs. time plotted in b), and $q$ vs. time plotted in c), all in body-frame coordinates**

For the Case 2 simulation, the body-frame coordinates of the projectile (see Fig. 2) are rotated by 45° to re-align the ${}^{B}Z$ and ${}^{W}Z$ axes when $\phi_A = 45°$. This body-frame coordinate change from the "+" to the "x" configuration consolidates all motion into the body pitch plane once more and facilitates a more direct comparison with Case 1. The simulation results for Case 2 in this "x" body-frame coordinate system are shown in Fig. 7. As the projectile is less stable in this orientation, the initial $q$ causes the projectile to pitch up to 15° before damping towards a steady state $\bar{\alpha}$ of about 6°. This behavior follows the trim analysis for $\phi_A = 45°$ from Fig. 4.

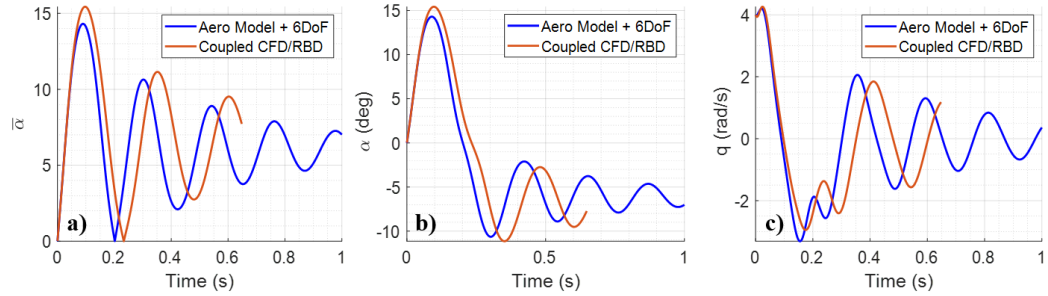


**Fig. 7 Flight simulation results for Case 2 at $\phi_A = 45°$, with $\bar{\alpha}$ vs. time plotted in a), $\alpha$ vs. time plotted in b), and $q$ vs. time plotted in c), all in "x" configuration body-frame coordinates**

## 5.3 Non-Rolling Flight

Following the pitch-constrained cases, another case is simulated in which the projectile dynamics are allowed to evolve in both the $\alpha$ and $\beta$ plane, while the projectile is prevented from rolling. As with Case 1 and 2, the projectile is launched at Mach 2 and initialized with a 4 rad/s pitch rate. The conditions for this simulation are given in Table 3.

**Table 3 Conditions for non-rolling simulation**

| | Initial conditions | | Aero forces and moments |
|---|---|---|---|
| Case 3 | $\phi_A = 0°$ | $q_0 = 4$ [rad/s] | $C_X, C_Y, C_Z, C_m, C_n$ |

The simulation results for Case 3 are shown in Fig. 8. The initial $q$ causes the projectile to pitch up in $\alpha$ to near 10° and oscillate between positive and negative $\alpha$, similar to the start of the Case 1 simulation. After about one pitch cycle, the $\beta$ plane motion begins to manifest, with $\beta$ leaving the unstable low angles of attack. The evolution of $\alpha$ and $\beta$ correspond to a transition from $\phi_A = 0°$ to a $\phi_A = 45°$ symmetry point, as shown in Fig. 8d, with the $\phi_A = 45°$ orientation shown again to be the least stable. The projectile motion eventually damps toward a steady-state trim of about 6° in $\bar{\alpha}$, as shown in Fig. 8a, which is expected from the trim analysis for $\phi_A = 45°$ from Fig. 4.

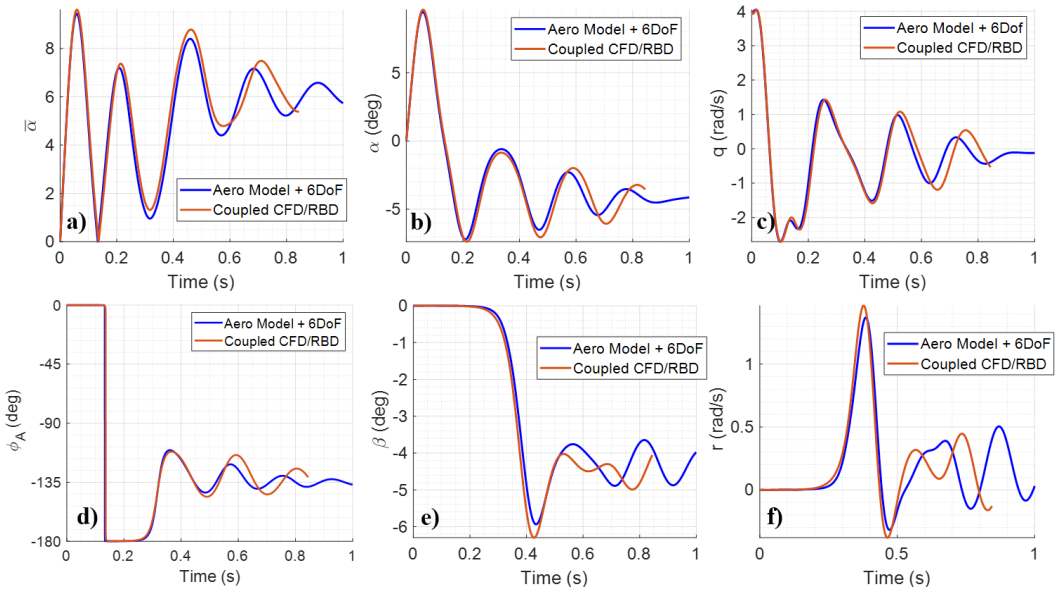


**Fig. 8 Flight simulation results for Case 3 at $\phi_A = 0°$**

## 5.4 Unconstrained Flight

The projectile is simulated with full, unconstrained dynamics using the 6DoF in a Monte Carlo analysis. A set of 30 simulations with both $q_0$ and $r_0$ are chosen from a normal distribution with $\sigma = 2$ rad/s, as described in Table 4. The results of these simulations are summarized in Fig. 9. The randomized initial q and r exercise the pitch and yaw motion, and munition transitions from $\phi_A = 0°$ to a $\phi_A = 45°$ symmetry point over time, as shown in Fig. 9e. The projectile motion eventually damps toward a steady-state trim of about 6° in $\bar{\alpha}$, with $\alpha$ and $\beta$ each trimming to about 4°.

**Table 4 Initial conditions for the Monte Carlo simulations**

| Initial conditions |
|---|
| $\phi_A = 0°$ |
| $q_0 = \mathcal{N}(0, 2^2)$ [rad/s] |
| $r_0 = \mathcal{N}(0, 2^2)$ [rad/s] |

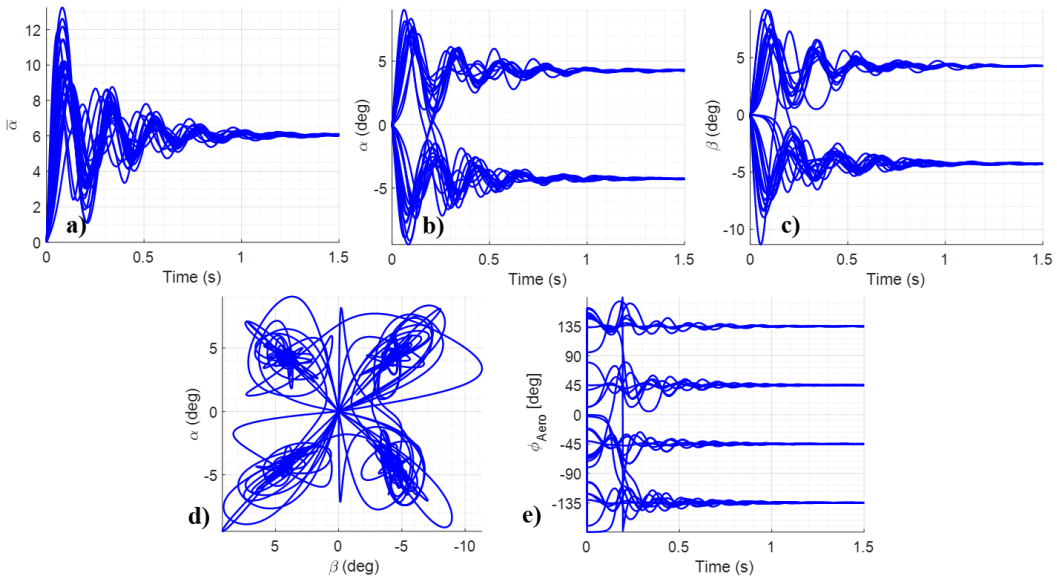


**Fig. 9 Results for the Monte Carlo flight simulations with unconstrained dynamics**

## 6. Conclusion

An aerodynamic model was presented and used to model a projectile with strong nonlinearities in static pitching moment due to angle of attack and aerodynamic roll angle. An aerodynamic trim analysis was presented using this aerodynamic model, indicating roll-dependency to the steady-state trim angles. The aerodynamic model was exercised using a 6DoF flight simulation, with complimentary analysis using (CFD/RBD) simulations. Pitch-isolated simulations were conducted and analyzed before adding yaw dynamics. These simulations demonstrated agreement between the CFD/RBD analysis and the modeled aerodynamics within the 6DoF flight simulation. Finally, a Monte Carlo set of unconstrained flight simulations using the modeled aerodynamics and 6DoF flight simulation was presented for analysis.

## 7. References


1. Costello M. Extended range of a gun launched smart projectile using controllable canards. Shock Vib. 2001;8203–213.

2. Fresconi FE. Range extension of gun-launched smart munitions. Proceedings of the International Ballistics Symposium; 2008; New Orleans, LA.

3. Bryson JT, Vasile JD, Celmins I, Fresconi FE. Approach for understanding range extension of gliding indirect fire munitions. Proceedings of the 2018 Atmospheric Flight Mechanics Conference; 2018 June 25–29; Atlanta, GA. AIAA 2018–3158.

4. Vasile JD, Bryson JT, Fresconi FE. Aerodynamic design optimization of long range projectile using missile DATCOM. Proceedings of the AIAA SciTech 2020 Forum; 2020 Jan 6–10; Orlando, FL. AIAA SciTech 2020–1762.

5. Pepitone TR. The influence of roll orientation-dependent aerodynamics on the stability of cruciform missile configurations. Dahlgren (VA): Naval Surface Weapons Center; 1981. Report No.: NSWC-TR-79-416.

6. Pepitone TR, Jacobson ID. Resonant behavior of a symmetric missile having roll orientation-dependent aerodynamics. J Guid Control Dyn. 1978;1(5):335–339.

7. Moore FG, McInville RM. Nonlinear aeroprediction methodology for roll positions of 45 degrees. J Spacecr Rockets. 1997;34(1):54–61.

8. Reece EW. Results of a wind tunnel test to determine the effect of roll position on the longitudinal static stability of the Tomahawk rocket configuration at Mach 7.3. Albuquerque (NM): Sandia National Laboratories; 1966. Report No.: SC-TM-66-495.

9. Bryson J, Vasile J, Gruenwald B, Fresconi F. Control surface design analysis and actuation requirements development for munitions. Proceedings of the AIAA SciTech 2020 Forum; 2020 Jan 6–10; Orlando, FL. AIAA SciTech 2020–0020.

10. McCoy RL. Modern exterior ballistics. Atglen (PA): Schiffer; 2012.

11. Fresconi FE, Celmins I, Silton S, Costello M. High maneuverability projectile flight using low cost components. Aerosp Sci Technol. 2015;41:175–188.

12. Zipfel PH. Modeling and simulation of aerospace vehicle dynamics. Reston (VA): AIAA Education Series; 2014.

13. Vasile J, Sahu J. Roll orientation-dependent aerodynamics of a long range projectile. Aberdeen Proving Ground (MD): CCDC Army Research Laboratory (US); 2020 Aug. Report No.: ARL-TR-9017.

14. Vasile J, Bryson J, Sahu J, Paul J, Gruenwald B. Aerodynamic dataset generation of a long range projectile. Aberdeen Proving Ground (MD): CCDC Army Research Laboratory (US); 2020 Aug. Report No.: ARL-TR-9019.

15. Costello M, Rogers J. BOOM: a computer-aided engineering tool for exterior ballistics of smart projectiles. Aberdeen Proving Ground (MD): Army Research Laboratory (US); 2011 June. Report No.: ARL-CR-670.

16. Peroomian O, Chakravarthy S, Goldberg U. A 'grid-transparent' methodology for CFD. Proceedings of the 35th Aerospace Sciences Meeting and Exhibit; 1997 Jan 6–7; Reno, NV. AIAA Paper 97-07245.

17. Peroomian O, Chakravarthy S, Palaniswamy S, Goldberg U. Convergence acceleration for unified-grid formulation using preconditioned implicit relaxation. Proceedings of the 36th AIAA Aerospace Sciences Meeting and Exhibit; 1998 Jan 12–15; Reno, NV. AIAA Paper 98-0116.

## List of Symbols, Abbreviations, and Acronyms

| | |
|---|---|
| 3-D | three-dimensional |
| 6DoF | six degrees of freedom |
| ARL | Army Research Laboratory |
| CCDC | US Army Combat Capabilities Development Command |
| CFD/RBD | computational fluid dynamics coupled to rigid-body dynamics |
| CG | center of gravity |
| CP | center of pressure |
| DOD | US Department of Defense |
| DSRC | DOD Supercomputing Resource Center |
| FAS | fixed aerodynamic surfaces |
| LTV | Laboratory Technology Vehicle |
| MAS | movable aerodynamic surfaces |
| RANS | Reynolds-averaged Navier-Stokes |

## Nomenclature

| | | |
|---|---|---|
| $\alpha$ | = | body angle of attack in pitch plane |
| $\bar{\alpha}$ | = | total body angle of attack, $\sqrt{\alpha^2 + \beta^2}$ |
| $\beta$ | = | body angle of sideslip in yaw plane |
| $C_{A_0}, C_{A_{\bar{\alpha}^2}}, C_{A_{\bar{\alpha}^4}}$ | = | zeroth, second and fourth order axial force coefficient |
| $C_{l_0}, C_{l_{\bar{\alpha}}}, C_{l_{\bar{\alpha}^2}}$ | = | zeroth, first and second order roll moment coefficient |
| $C_{l_p}$ | = | roll damping coefficient |
| $C_{N_0}, C_{N_{\bar{\alpha}}}, C_{N_{\bar{\alpha}^i}}$ | = | zeroth, first and i$^{th}$ order fit coefficients for normal force |
| $C_m$ | = | coefficient of pitching moment |
| $C_{m_0}, C_{m_{\bar{\alpha}}}, C_{m_{\bar{\alpha}^i}}$ | = | zeroth, first and i$^{th}$ order fit coefficients for static pitch moment |
| $C_{m_q}$ | = | coefficient of the pitch damping sum, including the $\dot{\alpha}$ term |
| $C_{n_0}, C_{n_{\bar{\alpha}}}, C_{n_{\bar{\alpha}^i}}$ | = | zeroth, first and i$^{th}$ order fit coefficients for static yaw moment |
| $C_{n_r}$ | = | coefficient of the yaw damping sum, including the $\dot{\beta}$term |
| $C_{S_0}, C_{S_{\bar{\alpha}}}, C_{S_{\bar{\alpha}^i}}$ | = | zeroth, first and i$^{th}$ order fit coefficients for side force |
| $D$ | = | reference diameter |
| M | = | Mach number |
| $p$ | = | roll rate |
| $\phi_A$ | = | aerodynamic roll angle |
| $q$ | = | pitch rate |
| $Q$ | = | ½ $\rho V^2$ , dynamic pressure |
| $r$ | = | yaw rate |
| $S$ | = | $D^2\pi/4$, aerodynamic reference area |

1 (PDF) DEFENSE TECHNICAL INFORMATION CTR DTIC OCA

1 (PDF) CCDC ARL FCDD RLD DCI TECH LIB

21 (PDF) CCDC ARL FCDD RLW A F E FRESCONI FCDD RLW LE J T BRYSON B C GRUENWALD J D VASILE J SAHU FCDD RLW L T SHEPPARD W OBERLE FCDD RLW LE B BURCHETT I CELMINS J DESPIRITO L FAIRFAX L STROHM FCDD RLW LB N TRIVEDI FCDD RLW LC J SADLER FCDD RLW LD A WILLIAMS FCDD RLW LF M ILG B TOPPER D EVERSON M HAMAOUI FCDD RLW LH B SORENSEN M MINNICINO